CHAPTER III

A detailed study on structural and optical properties of core TiO_2 and shell MgO in TiO_2-MgO nanostructures leading to enhanced photocatalytic activity in the core-shell nanostructure under daylight illumination

TiO_2 nanoparticles have caught the attention of researchers as an efficient and cost effective semiconductor which is used till date for various applications in the field of optoelectronics as well as photocatalysis. From the environmental aspect, it has become of utmost importance now a days to remove various dyes and pollutants that come together with wastewater from industries. So keeping the scenario of increasing environmental pollution in mind, we opted to work on this topic which was mainly based on two questions:

- ✓ Can TiO_2 nanoparticles synthesized via a simple laboratory method be used as an efficient photocatalyst?
- ✓ How does coating TiO_2 with another oxide material affect its optical and photocatalytic properties?

This chapter mainly deals in the properties of core TiO_2 and shell MgO along with the core-shell TiO_2-MgO. The structural, morphological and optical properties are studied via various characterization tools and a correlation among the properties of core and core-shell is tried to be established. The properties of the shell MgO are also extensively studied with an aim to see how the shell properties influence the property of the core-shell structure. We found no trace of shell characteristics as we go deep down tracking the optical properties of the core-shell indicating that only the core characteristics are enhanced /suppressed due to the addition of the coating layer. Although morphological property analysis clearly indicates the presence of the shell in the core-shell structure. An attempt to get inside temperature dependent optical properties of all three samples has been made as well.

3.1 Synthesis of TiO_2 nanoparticles

For the synthesis of TiO_2 nanoparticles, we followed a standard procedure [1]. Titanium iso propoxide was taken as the reactant and 2-Propanol as the solvent in a ratio 2:5.Then we allowed the solution to stir for 30 minutes followed by adding 1 drop of H_2O and left it for stirring upto 8 hours until gel formation occurs. Then the prepared gel was dried at 80^oC to remove the solvent and water portion from it. After drying, we got amorphous white powder and then annealed it at 430^oC to have the crystalline TiO_2 nanostructures.

3.2 Morphological properties

3.2.1 XRD pattern analysis

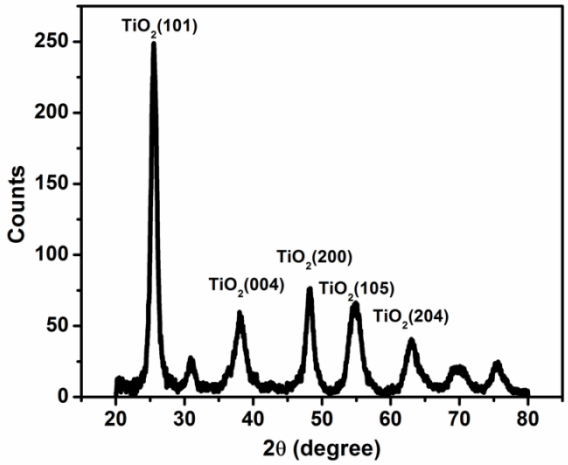

Fig. 3.1 XRD pattern of TiO_2 nanostructures

Synthesized TiO2 nanoparticles are characterized via XRD with peaks at positions of 2θ = (25, 38, 48, 54, 63, 69, 75) from different crystal planes {(101), (004), (200), (105), (204), (220), (215)}. All these peaks correspond to tetragonal anatase phase of TiO_2.The microstrain and crystallite size are also calculated from W-H plot which is listed in table 3.1. The strain is found to be positive. When the size of a material is reduced from bulk to nano, lots of defects occur and nanoparticles contain excess volume of atoms than that in the nanocrystallites. These excess atoms produce short range stress field and increases the lattice strain in the sample. The crystallite size is found to be 16.3 nm.

3.2.2 HRTEM characterizaion

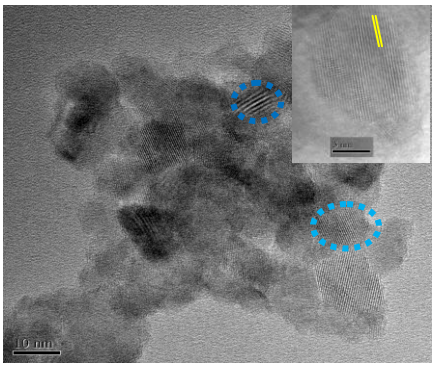

Fig. 3.2 TEM image of TiO_2 nanoparticles

Fig. 3.2 depicts the TEM image of TiO_2 nanoparticles. The blue colored circles show the lattice planes for the particles which are agglomerated owing to not adding any kind of surfactant during synthesis. The HRTEM image of a single TiO_2 nanoparticle is shown in the inset.

3.3 Optical Property Analysis

3.3.1 UV-vis absorption spectra

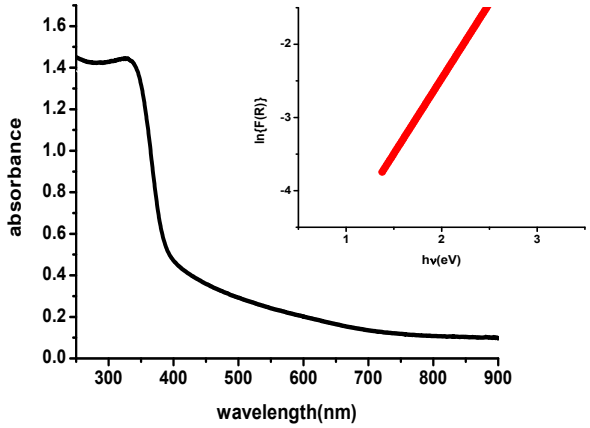

Fig. 3.3.1 UV-Vis absorbance spectra of TiO_2 nanoparticles (inset) Urbach tail Plot

Fig. 3.3.1 shows the UV-vis absorption spectra of TiO_2 nanoparticles. It is observed that the synthesized nanoparticles exhibit a loud peak around 340 nm along with a long tain in the visible region. This peak is the band to band absorption peak. Fig in the inset depicts the Urbach tail present in the sample. Considering the idea from bulk TiO_2, the Urbach tail is linked with the excitons self trapping, which is in agreement with the anatase phase as it has lower coordination among TiO_6 octahedra [2]. The Urbach equation is represented by

$$\alpha = \alpha_0 \exp (E/E_\mu) \qquad (3.1)$$

where, α is the absorption coefficient, E is the photon energy and E_μ is the Urbach energy. For the calculation of Urbach energy, lnα is plotted against E. The reciprocal of the slopes of linear portion, below optical band gap, gives the value of E_μ. Since absorption coefficient α is proportional to absorbance A (or F(R) in DRS mode), we can plot ln[F(R)] vs. photon energy, E [3-4]

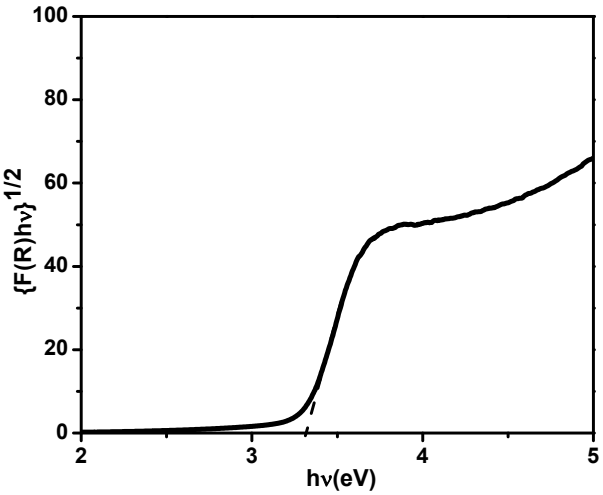

Fig. 3.3.2 Tauc's Plot for TiO_2 nanoparticles

The absorption is calculated by Kubelka-Munk plot $F(R) = (1-R)^2/2R$, where R is the reflectance of the sample and it is found from the reflectance spectra. The band gap of the nanomaterials were calculated from a plot of the modified Kubelka-Munk function $[F(R)E]^{1/2}$ vs the energy of absorbed light E (=hυ) where $R=R_{sample}/R_{BaSO4}$. After plotting the graphs and fitting linear, we get the band gap of TiO_2 nanoparticles to be 3.25 eV. The value is greater than that of bulk TiO_2 which is 3.2 eV. The increase in band gap in the nanoparticles can be attributed to quantum confinement effect which occurs due to transformation from bulk to nano.

3.3.2 Photoluminescence Spectra

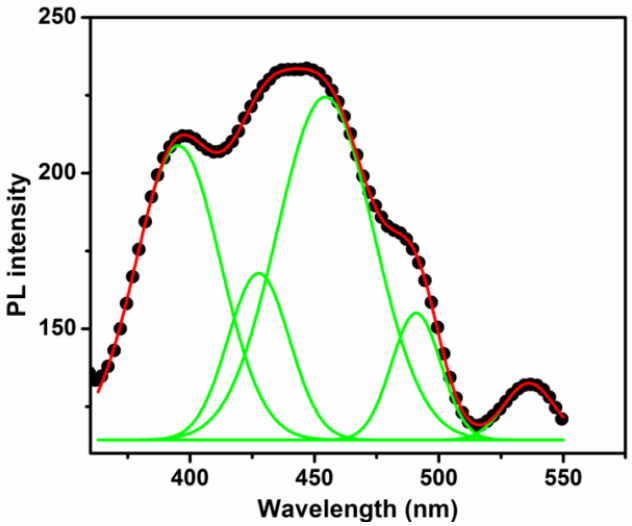

Fig. 3.4 PL spectra of TiO_2 nanoparticles.

Fig. 3.4 depicts the photoluminescence spectra of TiO_2 nanoparticles annealed at 450^{o}C. The strong emission peak around 390 nm occurs owing to phonon assisted indirect transition from M→Γ in the Brillouin zone. The visible emission peaks are accredited to excitons, oxygen vacancies and different surface defect states [5-6]. The oxygen defect related emission peaks are at 464 nm and 539 nm. These peaks are accredited to F or F ++ and F +centers respectively. The emission peak at 2.52 eV (492 nm) is due to charge transfer transition from Ti3+ to TiO_6^{2-} complex, associated with oxygen defects .The 425 nm peak is attributed to self trapped exciton emission [68-69].

3.4 Synthesis and characterization of shell MgO

3.4.1 Preparation of nanoscale MgO

The chemicals used for the preparation of MgO were magnesium nitrate hexahydrate (Merck, purity ≥ 99 %) and sodium hydroxide, NaOH (Merck, purity ≥ 97 %). Magnesium nitrate solution of 0.1 molar (M) was prepared in 100 mL double distilled water and stirred for 15 min, keeping the solution temperature at 50 ^{0}C. After 15 min 0.2 M NaOH solutions were added into it in the stirring condition [7]. White precipitate appeared at the end of the stirring for 3 h. The precipitate was washed with double distilled water and ethanol respectively. For washing the solution was taken in a 50 mL centrifuge tube and centrifuged at 6000 rpm. After first washing with water the product at the bottom of the centrifuge tube was sonicated in ethanol and then again centrifuged. The process of washing was continued for 3 times first with water followed by ethanol. The product was kept in a hot air oven maintained at 80^{o}C. The sample became completely dry after 10 h. The powder was then kept in a tube furnace with an initially temperature of 25^{o}C. After putting the sample the furnace is switched on. The furnace temperature reached 600^{o}C at a heating rate of ~0.2 sec/degree. We kept the sample in the furnace for 3 h for annealing and after 3 h the furnace was switched off. The sample was kept inside until the furnace temperature reached 25^{o}C. The sample was then taken out of the furnace and kept in container. The sample was labeled Mg600.

3.4.2 Structural and morphological study

3.4.2.1 XRD pattern analysis

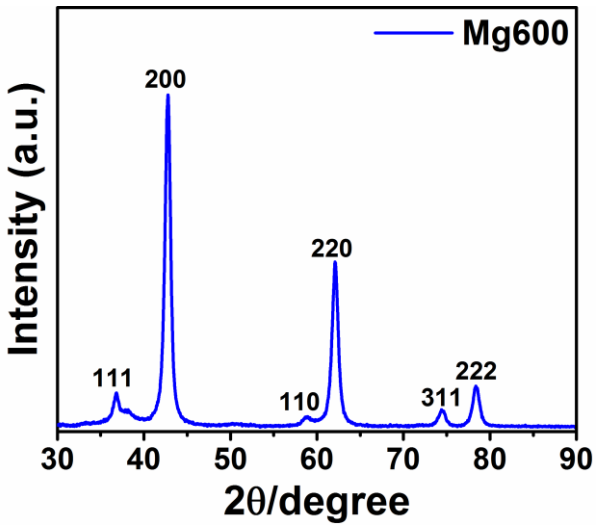

Fig. 3.5 XRD pattern of MgO nanoparticles.

X-ray diffraction pattern of Mg600 is shown in the above Fig. 3.5. The diffraction pattern corresponds to the face centered cubic lattice of MgO having space group $F\,m\,\bar{3}\,m\,(225)$ (JCPDS-89-7746). Mg600 contains a small peak at 2θ = 58.69 ^{0} corresponding to (110) peak of $Mg(OH)_2$ (JCPDS-860441). Presence of $Mg(OH)_2$ peak infers that the sample may contain hydrogen related impurities. These hydrogen related impurities could be formed when the –OH from $Mg(OH)_2$ interacts with oxygen vacancies present in MgO [MgO paper, 8] . The possible role of hydrogen impurities on the emission of MgO will be discussed latter. The crystallite size is calculated using Scherrer's formula in the Eva software equipped with the X-ray diffractometer. The Scherrer's formula is represented by

$$d = 0.9\lambda / \beta Cos\theta \qquad (3.2)$$

Where, d is the crystallite size, λ is the wavelength of X-ray radiation, β is the full width at half maximum and θ is the diffraction angle. We considered intense (200) diffraction peak for the determination of the crystallite size. The calculated crystallite size is 10.7 nm.

3.4.2.2 TEM image analysis

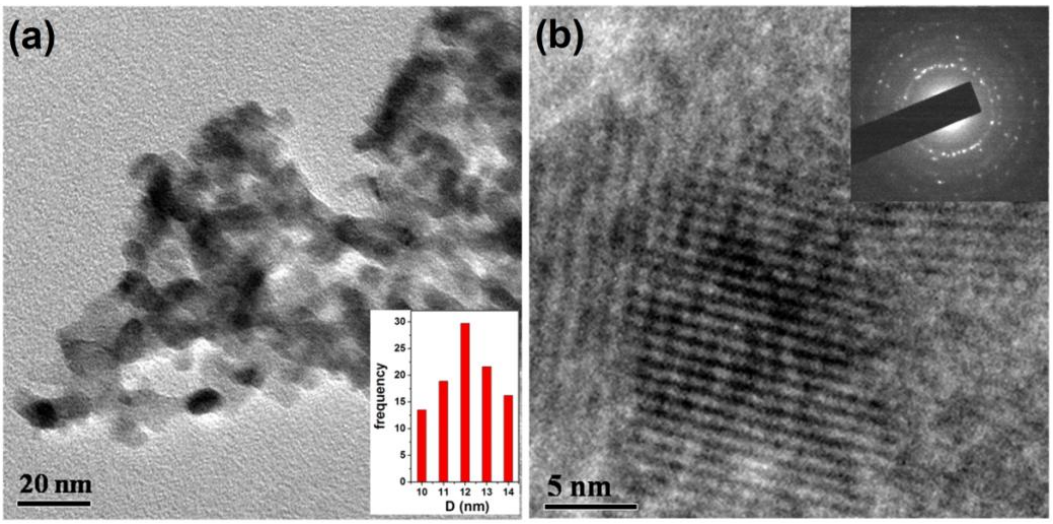

Fig. 3.6 (a) Low resolution TEM and (b) HRTEM image of MgO nanoparticles

Transmission electron microscope images of Mg600 are shown in Fig. 3.6(a-b). Fig. 3.6 (a) shows that the particles are agglomerated and are of varied shape. Inset of Fig. 2a shows the histogram displaying size distribution of the nanoparticles with average size of 12 nm. The crystalline nature of the prepared nanoparticle is confirmed from the observation of the clear lattice planes in Fig. 3.6 (b) and from the selected area electron diffraction (SAED) pattern shown in the inset of Fig. 3.6 (b).

3.4.3 Optical Property analysis

3.4.3.1 UV-Vis absorption study

Kubelka-Munk absorption plot and the corresponding reflectance spectra of Mg600 are shown in Fig 3.7 (a-b). Kubelka-Munk absorption or $F(R)$ is obtained from reflectance R considering the equation, $F(R) = (1\text{-}R)^2/2R$, where R is reflectance of the sample. The lower spectral detection limit of the UV-vis spectrophotometer is 200 nm. Therefore, we could not detect any absorption or reflectance below 200 nm. The

UV-vis spectral range from 280-700 nm are Gaussian fitted with fitting correctness, r^2= 0.9985 (shown inset of Fig. 3a).

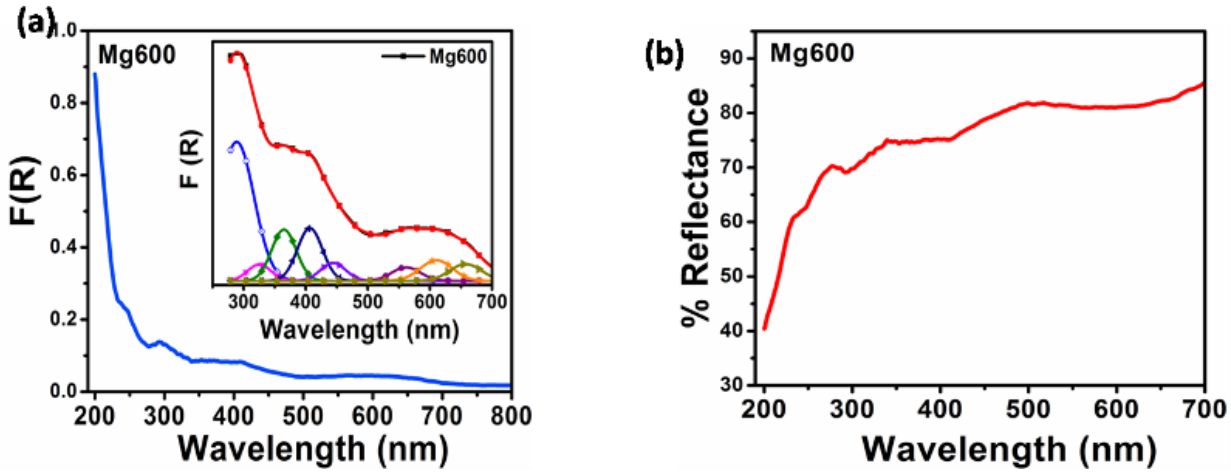

Fig. 3.7 (a) Kubelka-Munk absorption plot and (b) Reflectance spectra of MgO.

For bulk MgO the absorption threshold could be seen at 7.8 eV in the UV region [9]. However, nanocrystalline MgO contains several absorption peaks in the UV and visible region. Those absorptions are due to the presence of defects and low coordinated cations and anions on the surface, interface, etc. [10-11].

The absorption at ~ 200 nm (6.2 eV) involves excitation of 5 coordinated surface anions [9, 12]. In the present study the observed absorption at 250 nm (4.96 eV) could be associated with bulk F or F^+ centers [13]. The absorption at 289 nm (4.29 eV) is owing to singlet to singlet $^1A_{1g}$ to ^1E transition of electrons present in the surface F_s center [14]. The other singlet to singlet $^1A_{1g}$ to $^1A_{1g}$ excitation of surface F_s center is observed at 405 nm (3.06 eV). These two singlet to singlet transitions of surface F_s center arises owing to crystal field splitting of the 2p states of oxygen defect on the surface [14]. The absorption peak at 652 nm (1.90 eV) involves singlet to triplet photoexcitation of electrons from ground $^1A_{1g}$ state to excited $^3A_{1g}$ state of surface F_s center [14]. The absorption peak at 365 nm (3.39 eV) is due to the surface F_s^+ center and involves $^2A_{1g}$ to $^2A_{1g}$ electronic transition [14]. The absorption peak at 324 nm

(3.83 eV) is due to F_2^{2+} centers [15-16]. The dimmers or aggregates of *F* centers are formed by the pairing of the nearest *F* centers (*F*, F^+ or F^{2+}). Thus, depending on the number of trapped electrons by the paired oxygen vacancies these aggregates are referred as F_2 (with four electrons), F_2^+ (three electrons), F_2^{2+} (two electrons in two vacancies) respectively [16]. The absorption peak at 559 nm (2.21 eV) is likely due to V^- center [17-18]. V^- center consists of a single hole trapped oxygen ion adjacent to a magnesium vacancy having the configuration O^{2-}-[$Mg_{vacancy}$]-O^- [19]. The absorption at 444 nm (2.79 eV) is due to the transition of a four coordinated *F* center [20-21]. The absorption at 605 nm (2.05 eV) appears owing to 5-coordinated surface F_s^+ centers [22-23]. In the present discussion the notation corresponding to surface or bulk *F* or F^+ centers is provided based on the theoretical work by Illas *et al.* [14]. He studied the possible absorption positions of bulk and surface *F* centers in MgO. He stated that *F* and F^+ centers have higher coordination (O_h symmetry) in the bulk and lower coordination (C_{4v} symmetry) with the surrounding ions on the surface [14]. In bulk MgO the absorptions are mostly due to bulk *F* centers. However, because of the nanoscale size Mg600 contains higher percentage of *F* or F^+ centers on the surface. Because of the different symmetry and due to different extent of the crystal field splitting of the 2*p* states on the surface than in the bulk, the *F* or F^+ centers on the surface show different absorptions than in the bulk.

3.4.3.2 Photoluminescence (PL) study

PL spectra of MgO are taken at three different excitations, 206 nm, 270 nm and 330 nm respectively. The emission spectra of MgO at λ_{ex} = 206 nm is shown in Fig. 3.8a. Excitation at this wavelength generates several emission peaks with the intense emission lying in the UV region centering at 365 nm. Fig. 3.8b shows the excitation spectra monitored at 365 nm emission. The excitation spectra contain peaks at 225 nm, 245 nm and 262 nm. The excitation peak at 225 nm may be assigned to bulk *F* centers, whereas the peaks at 245 nm and 262 nm correspond to *F* and F^+ centers respectively [12, 13, 23]. Therefore, the intense emission at 365 nm may be due to *F* or F^+ center. However, reports suggest that emission due to *F* centers appear in between 416-420 nm and at ~ 516 nm, whereas emission due to F^+ center lies in between 390-400 nm [14, 24]. Therefore, the emission at 365 nm may be assigned to F^+ center with its

corresponding excitation at 262 nm. Photoexcitation at 206 nm results in the excitation of the F^+ center electrons leaving a ground state F^{2+} center and electrons in the conduction band. During emission the conduction band electron encounters with F^{2+} giving 365 nm emission, $F^{2+}+e^- \rightarrow F^+ + h\upsilon$ (365 nm) [14]. The emissions in between 280-320 nm may be due to energy transfer from one anion to another present on low coordination sites on the surface [25].

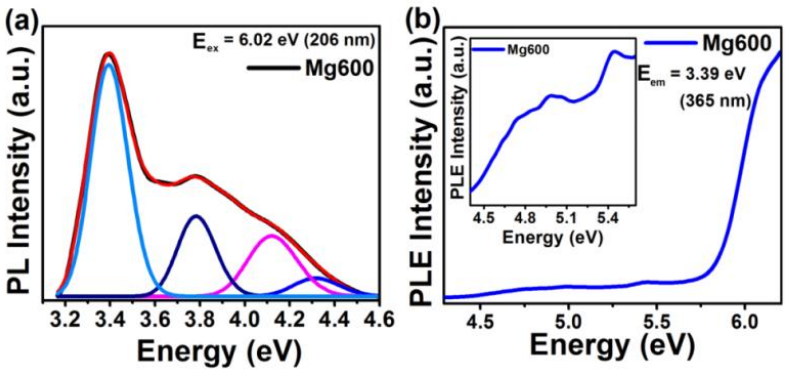

Fig. 3.8 Photoluminescence spectra of MgO excited at (a) 206 nm. (b) PLE spectra monitored at the intense emission, λ_{ex} = 365 nm. Inset shows the extended spectra in the range from 220-280 nm to show the excitation peaks.

Photoluminescence spectrum of MgO nanoparticles, excited at 270 nm, is displayed in Fig. 3.9a. Excitation at 270 nm results in emission peaks at 345 nm, 359 nm, 375 nm, 390 nm, 407 nm, 427 nm and 446 nm, 464 nm and 491 nm with intense emission being at 427 nm.

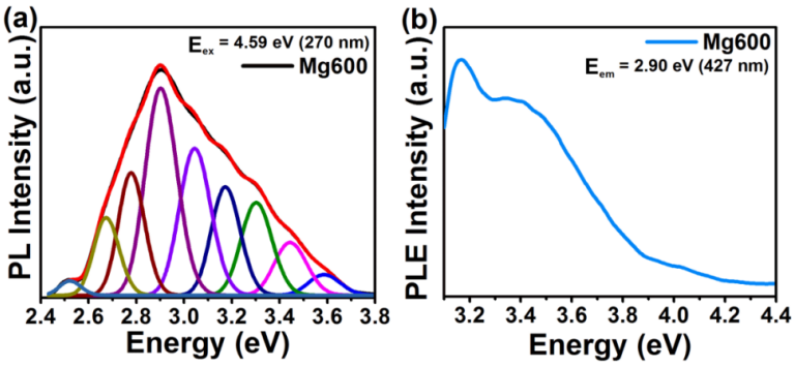

Fig. 3.9 Photoluminescence spectra at (a) λ_{ex} = 270 nm. (b) PLE spectra monitored at the intense emission 427 nm.

The PLE spectra (Fig. 3.9b) monitored at 427 nm results in excitation peak at 365 nm and 390 nm along with a small excitation at 310 nm. The absorption at 365 nm and 390 nm may be associated with F_2 centers [12, 14]. The absorption peak at 310 nm is due to F_2^{2+} centers [12]. The corresponding emission spectra of F_2 centers and F_2^{2+} centers appear at 375 nm and 475 nm respectively [23]. F_2^{2+} center in MgO has a D_{2h} point symmetry and consist of F^+ centers in nearest neighbour anion sites along <110> lattice direction [23]. Kumar et al. observed F_2^{2+} center related emission peaks in between 425-443 nm [14]. Therefore, the intense emission in the violet region at 427 nm may be assigned to $^3B_{1u}$ to $^1A_{1g}$ transition of electrons in F_2^{2+} center with its corresponding excitation at 310 nm [14]. Fig. 3.10a shows the PL spectra of MgO excited at 330 nm. Excitation at this wavelength gives an intense emission peak at 419 nm. This 419 nm emission peak is due to *F* center. The corresponding PLE spectra monitored at this intense emission, shown in Fig. 3.10 b, gives an excitation peak at 228 nm. This excitation peak is due to bulk *F* center [12]. Rosenblatt and his co-workers attributed the emission peak at 530 nm to *F* centers [25].

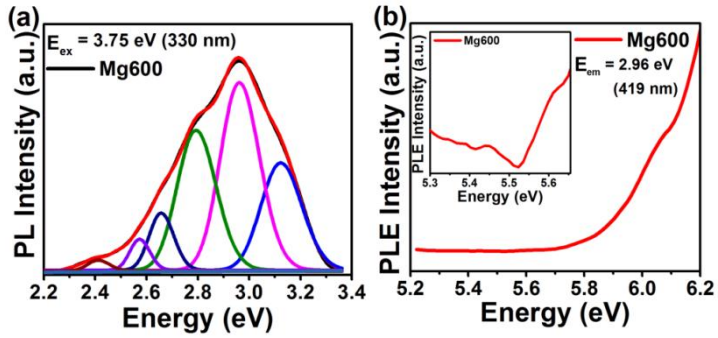

Fig. 3.10 Photoluminescence spectra at (a) λ_{ex} = 330 nm. (b) PLE spectra monitored at λ_{em} = 330 nm. Inset shows the extended spectrum to display the excitation peaks.

On the other hand, Kawaguchi et al. observed F^+ and *F* center related emission peaks at 430 nm and 500 nm in the fracto-luminescence study of MgO single crystals [26]. Boubeta et al. attributed the 420 nm emission peak to *F* center in defective MgO film [16]. Since our PLE spectrum corresponding to 419 nm shows an excitation peak at 228 nm, which is due to bulk F center, we can assign the intense emission peak to bulk *F* center [12]. The other emission peak at 514 nm may also be assigned to bulk *F* center [25-26].

Apart from the intense emission peaks in the near UV or violet region, excitation of MgO at 206 nm, 270 nm and 330 nm result in several other emission peaks lying in the blue and green regions of the visible spectrum. Those emission peaks lie in between 441-446 nm (violet), 461-486 nm (blue) and at 514 nm (green). The emission peaks in the range ~ 441-446 nm are due to F_2^{2+} center and the emission peaks in between 461-464 nm may be assigned to hole trapped at Mg ion vacancy [16]. The emission lying in between 474-479 nm is assigned to F_2^{+} center and the emission lying at 491 nm is due to hydroxyl group adsorbed at the low coordination site on the surface [16, 23].

3.4.3.3 Temperature effect on the emission spectra:

In order to understand the effect of high temperature air annealing on the intensity of emission peaks, one part of the as prepared MgO is annealed at 800 ^{0}C for 3 h. This sample is labeled Mg800 and the crystallite size of the sample is 20 nm. As evident from Fig. 3.12-c, irrespective of the excitation energy, the emission intensity of MgO appears to be reduced on annealing at 800 ^{0}C. We have plotted the intensity ratio of F^+/F, F_2^{2+}/F^+ and F_2^{2+}/F as a function of annealing temperature.

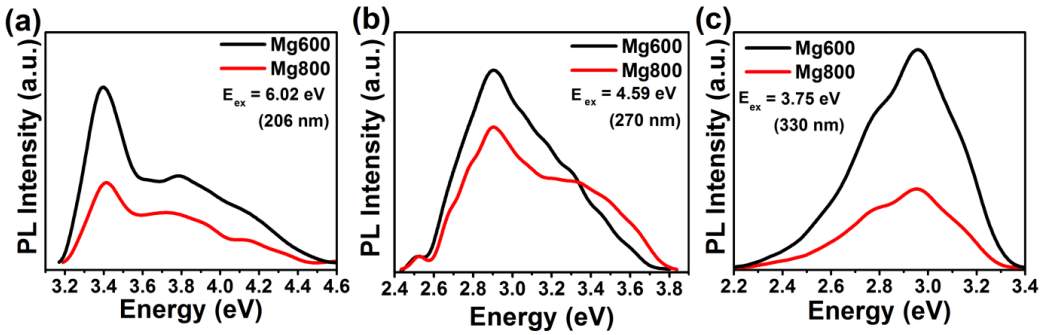

Fig.3.11 Photoluminescence spectra of MgO annealed at 600°C and 800°C and excited at (a) 206 nm (b) 270 nm and (c) 330 nm

The intensity ratios for different emissions were determined based on emission spectra decomposition by Gaussian fitting. The intensity ratio of F^+/F decreases at 800°C as shown in Fig. 3.12a. Edel *et al.* observed photoconversion of F to F^+ center on excitation at 4.96 eV (250 nm). They also stated that thermal treatment may convert F^+ to neutral F centers [27]. We have observed that photoexcitation of MgO at 4.59 eV (270 nm) and 3.75 eV (330 nm) result in the transformation of a considerable numbers of F centers to F^+ centers, following the process $F+h\nu \rightarrow F^+ +$ (emission). Thus, F^+

emission seems to be enhanced in comparison to *F* center emission at 600^{o}C. On the other hand the F^+/F intensity ratio decreases at 800^{o}C. At 800^{o}C most of the F^+ centers might have been converted to *F* centers [28-30]. This F^+ to *F* center conversion is reported to be assisted by H^- impurities at high temperature. Thermal conversion increases the population of *F* centers and thus, enhances the intensity of *F* center emission, with subsequent reduction in F^+/F intensity ratio. Fig. 3.12b displays the intensity ratio of F^+ to F_2^{2+} emission centers. Whether it is 4.59 eV (270 nm) or 3.75 eV (330 nm) excitation, the F^+/F_2^{2+} emission intensity ratio decreases on annealing MgO at 800^{o}C. Decrease in the intensity ratio at high temperature indicates quenching of the intensity of F^+ emission as compared to that of F_2^{2+} emission. Since F_2^{2+} aggregates are formed by the association of nearest F^+ centers, the numbers of these aggregates depend on the concentration of F^+ centers. Thermal annealing at 800^{o}C results in the conversion of F^+ centers to *F* centers. Hence, emission intensity of the F^+ center decreases in response to the intensity of the F_2^{2+} centers. Excess F_2^{2+} aggregates might not be produced at 800^{o}C, but due to reduction in the number of F^+ centers the F^+/ F_2^{2+} intensity ratio is believed to be reduced. Even if we consider that thermal annealing dissociates F_2^{2+} into F^+ centers, the process of photoconversion of F^+ to *F* centers will be faster than the dissociation rate of the aggregates to F^+.

Thus, we can consider that the number of F_2^{2+} ions participating in the emission will be higher than those of F^+ ions and that is why we have observed decrease in the intensity ratio of F^+/F_2^{2+} at 800^{o}C. Fig. 8c shows the intensity ratio of F/F_2^{2+} as a function of temperature. It is seen from the figure that thermal annealing increases the F/F_2^{2+} emission intensity ratio at 800^{o}C. This indicates that F_2^{2+} emission intensity decreases at high temperature in comparison to *F* center emission. This is quite obvious since thermal annealing is likely to dissociate F_2^{2+} to F^+ center (although the process is not as fast as F^+ to *F* conversion) and finally these F^+ transforms into *F* centers. Therefore, the numbers of these *F* centers are expected to be higher than F_2^{2+}, resulting in the enhancement of F/F_2^{2+} intensity ratio at 800^{o}C.

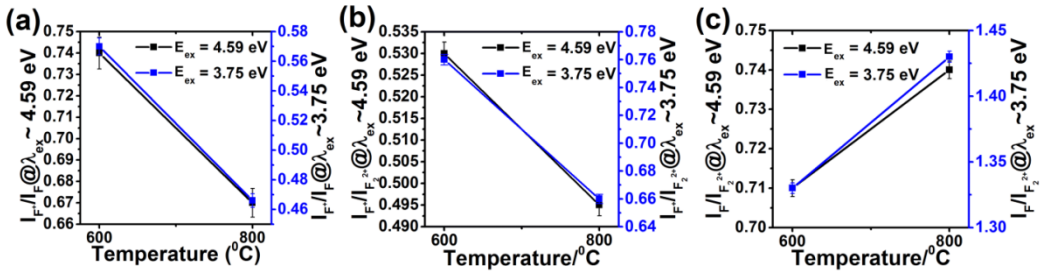

Fig. 3.12 Plot of the intensity ratio of defect emissions as a function of annealing temperature for (a) F^+/F (b) F^+/F_2^{2+} and (c) F/F_2^{2+} at 270 nm and 330 nm excitation.

3.5 Synthesis of core-shell TiO_2-MgO nanostructures

The TiO_2 nanoparticles were synthesized as we have described in section 3.1. The obtained TiO_2 nanoparticles were annealed at three different temperatures namely 450°C, 650°C and 850°C**.** The coating layer was prepared by adding NaOH solution to Magnesium nitrate hexahydrate solution as described in section 3.4.1. Thus we obtained a coating of $Mg(OH)_2$ layer over the TiO_2 core followed by drying the sample at 100°C to remove the water portion for having a shell MgO. We added the coating layer separately to the three core samples annealed at different temperatures to get the core-shell nanostructures labeled as TM 450, TM 650 and TM 850.

3.6 Structural and Morphological Properties of core-shell TiO_2-MgO

3.6.1 XRD analysis

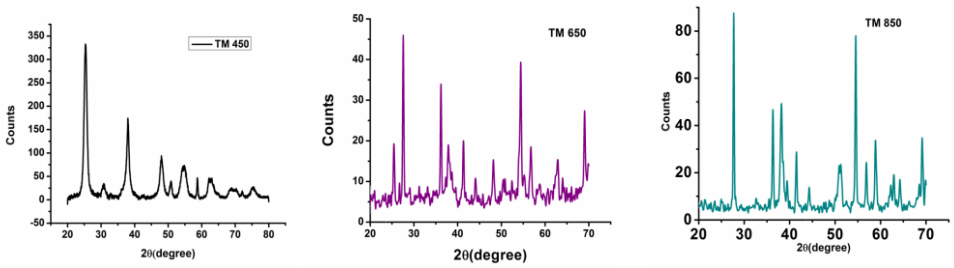

Fig. 3.13 XRD pattern of core-shell TiO_2-MgO nanostructures with core annealed at (left) 450°C, (centre) 650°C and (right) 850°C.

Fig. 3.13 shows the XRD pattern of the core-shell nanostructures while the core was annealed at different temperatures. TM 450 shows peak positions at 2θ = (25, 38, 48, 54, 63, 69, 75) from different crystal planes {(101), (004), (200), (105), (204), (220), (215)}. All these peaks correspond to tetragonal anatase phase of TiO_2. The XRD patterns indicate that none of the coatings affected the TiO_2 composition as there is no apparent shift in the existing peaks assigned to rutile and anatase phases. We believe that the thickness of the coating layers consist of a few nanometers, this would explain why no peaks from these layers were detected [31].The rutile peak of TiO_2 (110) i.e 2θ = 28 occurs at both TM 650 and TM 850. Thus TM 450 exhibits all the anatase peaks like its core counterpart. In TM 650 and TM 850, presence of rutile phase can be found along with complete quenching of the (101) peak that occurs at $2\theta = 25^o$ in TM 850. The crystallite sizes and microstrain were calculated from W-H plot and are tabulated below in table 3.1.

Table 3.1 Calculation of crystallite size and microstrain

Sample name	**Crystallite size(nm)**	**Microstrain**
TiO_2	16.3	0.0053
TM 450	33	0.01145
TM 650	39	0.0013
TM 850	39.3	0.0085

From the table 3.1, we can see that the crystallite size of TM 450 is much more than pure TiO_2 indicating the coating layer formation surrounding the core. Also with increase in annealing temperature of the core, the crystallite size increases as there is enlargement of grain boundary with temperature. Oxygen vacancies, defects on the surface and on the grain boundary, impart a positive strain in the lattice of TiO_2 nanocrystallites annealed at 450^oC. In the core-shell TM 450, as we have observed the microstrain is enhanced than the core counterpart. This may be attributed to the reason that upon addition of the coating layer to the core, a significant lattice mismatch occurs at the interface of the core and shell hereby increasing the strain. Again the oxygen

vacancy related defects are enhanced in the core-shell structure than the core structure which also plays a vital role in increasing the microstrain in the core-shell system. As we go on annealing the core at 650^{o}C, many of the grain boundary defects are reduced and promote movement of atoms from grain boundary to the grain interior [32]. Removal of grain boundary defects decreases the stress field in this regime with a successive reduction in the magnitude of lattice strain. But in case of annealing at 850^{o}C, the strain is again increased as the core size becomes sufficiently large than the volume of the shell (the shell concentration is same in all cases, so when the core expands the shell may get compressed) hereby imparting significant strain on the shell resulting in enhancement of the microstrain in the TM 850 system.

3.6.2 TEM image analysis

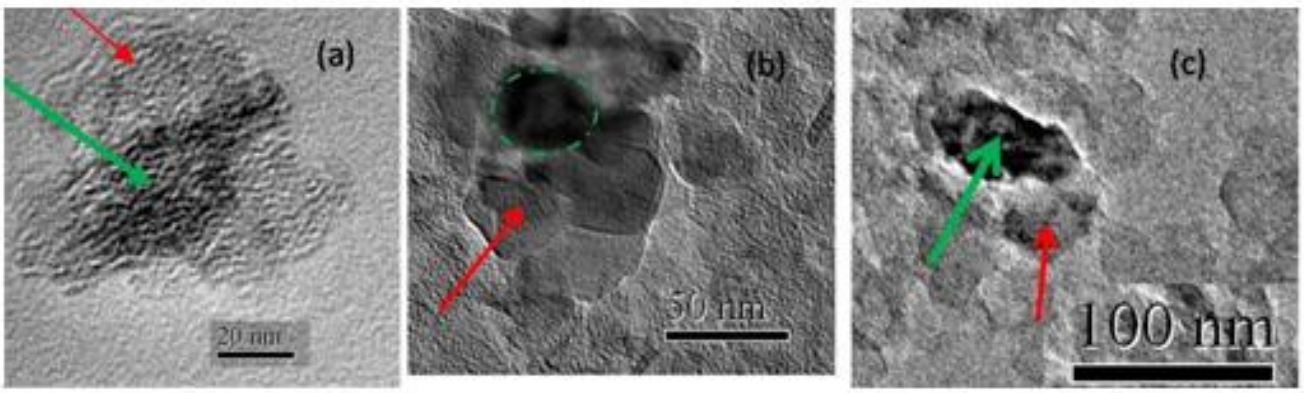

Fig. 3.14 TEM images of TiO_2-MgO nanostructures annealed at (a) 450^{0}C (b) 650^{0}C and (c) 850^{0}C

Fig. 3.14 portrays the TEM images of all the three core-shell heterostructures annealed at 450^{o}C, 650^{o}C and 850^{o}C respectively. The green colored shapes (arrow and circles) indicate the core portion in the sample while the blue colored arrows do the same for surrounding shell layer. It was not possible to find any single core-shell nanoparticle due to huge agglomeration present in the sample, but one thing is clear from the images that significant increase in particle size is prominent as we go on increasing the annealing temperature of the core particles.

3.6.3 EDX spectra analysis

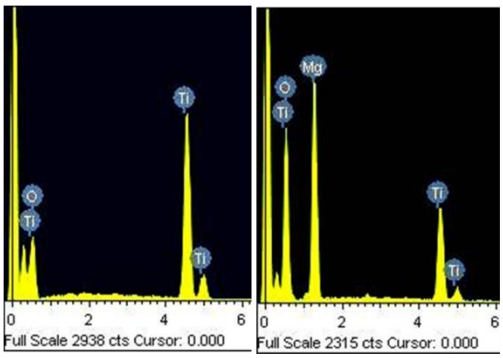

Fig 3.15 EDX pattern of (left) TiO_2 and (right) TiO_2-MgO

The EDX spectra of the samples are shown in fig. 3.16 which confirms the presence of all the constituent elements Ti, Mg and O in the sample.

3.6.4 FTIR spectra

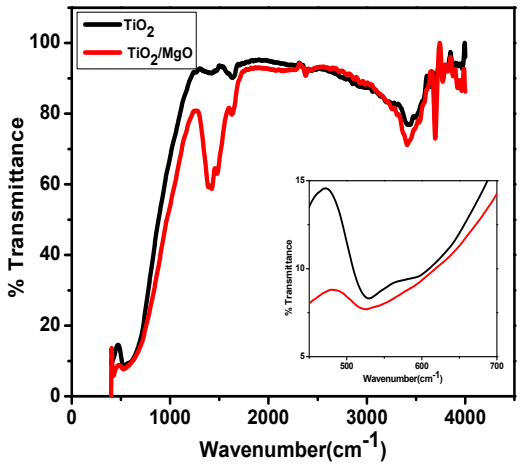

Fig. 3.16 FTIR spectra of both core TiO_2 and core-shell TiO_2-MgO nanostructures. Extended version of the Ti-O bond (inset)

Fig. 3.16 represents the FTIR spectra of both core TiO_2 and core-shell TiO_2-MgO nanostructures. The broad band centered at 500-600 cm^{-1} is likely due to the vibration of the Ti–O bonds in the TiO_2 lattice. The peaks at 1620-1630 cm^{-1} and the broad peaks appearing at 3100–3600 cm^{-1} are assigned to vibrations of hydroxyl groups.

Also it is observed that the position of Ti-O bond is shifted to lower frequency regime resulting in broadening of the peak.

$$\acute{\upsilon} = \frac{1}{2\pi C}\ (\sqrt{k/\mu}) \qquad (3.3)$$

The FTIR frequency shifting can be determined from the above equation. The broadening of the peak may be accredited to the generation of defects owing to mismatch of bonds at the interface [33]. In pure TiO_2, the position of Ti-O bond is determined by its strength or by its force constant. After incorporation of MgO to TiO_2, the amount of oxygen vacancy is increased, which is further explained with XPS spectra. Hence, there will be less O atoms to form Ti-O bond in core-shell TiO_2-MgO. This results in weakening of the bond thereby lowering the force constant which explains the shifting of the bond towards lower wavenumber. The MgO coated TiO_2 possesses a larger amount of hydroxyl group 3600-3000 cm^{-1} as well as water molecules around 1624 cm^{-1} confirming that the MgO coating has a potential in photodecomposition of air pollutants as well. The role of these two species hydroxyl group and water molecule has been allegedly known as follows. The profusion in hydroxyl groups permits for more radicals on the surface, facilitating the decomposition process of organic materials. Regarding MgO coated TiO_2, the photogenerated holes from the TiO_2 core are simply assumed to reach the outer surface of ultrathin MgO shell via quantum tunneling to form a highly active hydroxyl radical [34].

3.6.5 Raman Spectra analysis

This spectroscopic technique is skilled to probe structures of gases, liquids and crystalline and amorphous solids [35-36].The Raman effect arises when an intense monochromatic radiation experience inelastic scattering on passing through a sample containing molecules resulting in the change in molecular polarizability on vibration [35-36]. When a sample is irradiated with incident light of frequency ν_o, the scattered light is shifted by frequency $\nu_o \pm \nu$. Raman scattering light undergoing a frequency shift ~ ν_o-ν (longer wavelength) are called Stokes light and scattered light with frequency shift ~ ν_o+ν (shorter wavelength) are known as anti-Stokes light. The anti-Stokes

intensity is much lower than the Stokes intensity. The frequency (or energy) shift is ascribed to the transfer of energy due to the lattice vibrations (phonon), molecular vibrations, rotation of molecules and electronic transitions [35-38].

The Raman spectra of TiO_2 and core-shell TM 450 samples are recorded using Renishaw In Via Raman spectrometer (Rensihaw, Wotton-under-Edge, UK) at a resolution of 0.3 cm^{-1} Ar^+ laser of 514.5 nm wavelength is used for excitation.

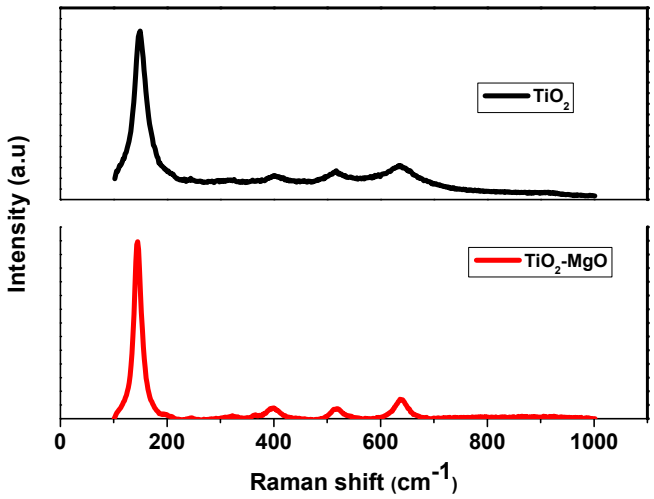

Fig 3.17 Raman spectra of both TiO_2 and TM 450

Raman spectra of both TiO_2 and TM 450 samples are shown in Fig. 3.16. Anatase TiO_2 has six Raman active modes and three infrared (IR) active modes. The optical phonon mode at the Γ-point of Brillouin zone (BZ) is presented by [39-40].

$$\Gamma = A1g(R) + 2B1g(R) + 3Eg(R) + B2u(IR) + A2u\ (IR) + 2Eu\ (IR) \qquad (3.4)$$

The four vibrations (*A1g+B1g+B2g+Eg*) are Raman active and the rest are IR active. In these samples, an intense *Eg* peak appears at 144 cm^{-1}, followed by low intense *A1g, B1g* peaks at 410 cm^{-1}, 520 cm^{-1} and at 630 cm^{-1} respectively [41-42].

Lattice strain, defects, crystallite size strongly influence the shifting, peak broadening and the intensity of the Raman peaks [43-44]. For pure crystal, the phonon contribution comes from the center of the Brillouin zone, at q = 0 [44-46]. However, for small nanocrystallites, the phonon dispersion counts on phonon contribution from

entire Brillouin zone [44,47]. The breaking of the phonon selection rule influences the Raman line shape, position, etc. [47]. Positive phonon dispersion from zone center will lead to asymmetric broadening, blue shift and reduction in the intensity of Raman peak [48].

To study the effect of size, defects and temperature on the position, width of the Raman peak, we have considered the *Eg* Raman peak. Xu et al. [48] employed a phonon confinement model to explain the observed changes in the Raman line and position using Heisenberg uncertainty principle.

$$\Delta X \, \Delta P \geq h/4\pi \qquad (3.5)$$

Where ΔX is particle size, ΔP is the phonon momentum distribution and h is Planck constant. In case of a perfect crystal first order Raman scattering of photons obey the phonon selection rule q=0, implying phonon contribution at the center of Brillouin zone. So, when ΔX increases as we can see in our case, ΔP decreases thus the phonon contribution becomes very less. This results in shifting as well as contraction of the active Raman peak. The red Raman downshifts are mainly ascribed to either size-induced phonon confinement [49] or lattice defects, such as point defects, dislocations and stacking faults [49]. Again the strength of a bond is determined by its force constant and the force constant of a bond is connected with frequency by $\upsilon \infty \sqrt{k}$ [50]. The increase in oxygen vacancies in the core-shell nanostructure plays a vital role in red shifting of the Raman peak as number of Ti-O bonds decrease due to lack of oxygen resulting in decreasing the force constant and thus the wavenumber also thus gets reduced.

We have calculated the phonon lifetime, considering *Eg* mode, in each sample by adopting the energy-time uncertainty relation, $\Delta E/\hbar = 1/\tau = 2\pi c\Gamma$, where ΔE is uncertainty in the energy of phonon mode, $\hbar$ is reduced plank constant, Γ is the FWHM of the Raman peak [45,51]. The calculated phonon lifetime (τ) are presented in table 3.2.

Table 3.2: Calculation of phonon lifetime

Sample	Raman line width of E_g peak (cm^{-1})	Phonon lifetime (pico sec)
TiO_2	23.64	0.19
TM 450	15.51	0.29

It is realized from the table that the phonon lifetime increases in case of the core-shell nanostructure. As we can see from table 3.1 that crystallite size of TM 450 is much higher than that of TiO_2 which leads to an increase in the phonon density and thus anharmonic phonon coupling increases. This finally increases the decay time or the lifetime of the phonons [51].

3.6.6 XPS spectra analysis

The principle of X-ray photoelectron spectroscopy is based on photoelectric effect. When a material is irradiated with X-ray photon with an energy *hυ*, the energy is absorbed by the core or valence electrons that are bound to the atoms with a binding energy of *EB*. If the absorbed energy *hυ* is very high the electrons will be excited and will leave an electron in the atom with kinetic energy *EK*. This energy is the difference between incident energy *hυ* and the binding energy *EB* i.e. $EK = h\upsilon - EB$ [52-53].

When applied to solids, XPS is a surface sensitive technique. The nominal analysis depth is on the order of 1 to 10 nm (10 to 100 monolayers) [52-53]. The sensitivity of XPS for the detection of elemental composition is 0.1 at %. However, the sensitivity varies for different elements and for different concentration of the elements [53]. In analysis of solid materials, the two primary uses of XPS are to determine elemental compositions and to characterize the chemical states of elements. Other applications include determining film thickness or composition profiles at the surface of a material, either through nondestructive or destructive means, and characterizing molecular orientation for adsorbates on surfaces [53].

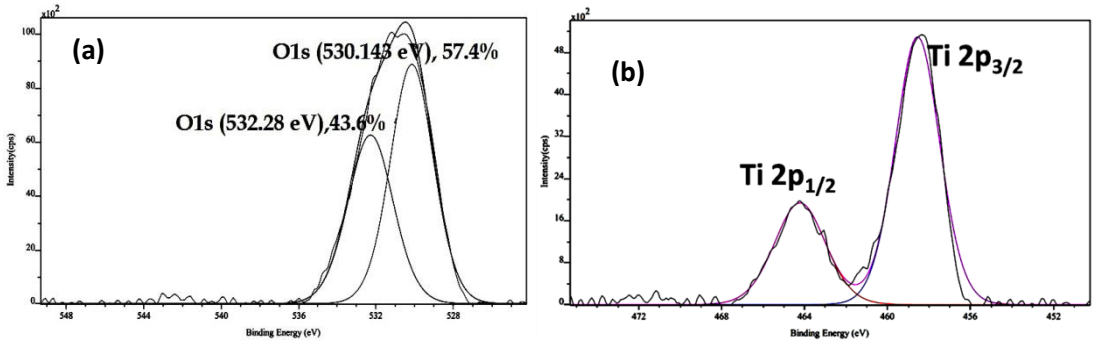

Fig. 3.18 XPS of TiO_2 nanoparticles (a) O1s (b) Ti 2p spectra

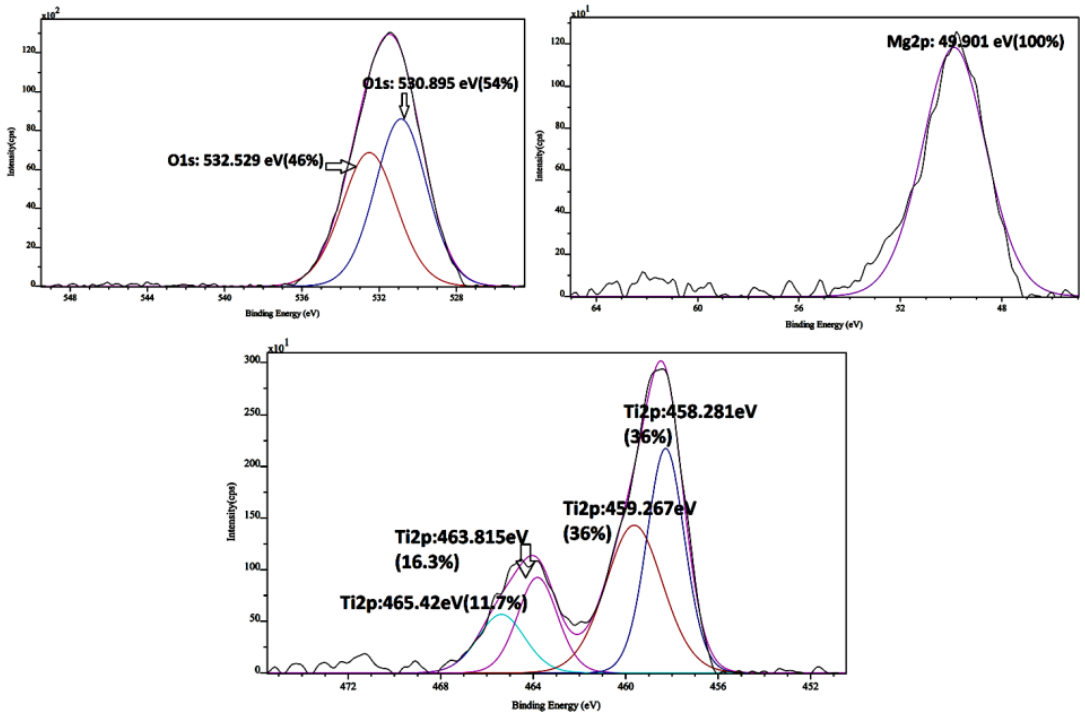

Fig. 3.19 XPS of core-shell TiO_2-MgO nanoparticles

Fig. 3.19a shows the XPS spectrum for pure TiO_2 nanoparticles. The O1s spectrum is deconvoluted to 2 peaks. The 530.143 eV peak corresponds to O_L that is oxygen in the TiO_2 crystal lattice whilst the 532.28 eV peak is assigned to O_H that is due to the presence of hydroxyl atoms. It can be seen that the intensity of the O_L peak is decreased in the core-shell structure indicating that there is more oxygen vacancy in the sample than its core counterpart. Again both O_L and O_H peaks are shifted to higher binding energies and this shift may be attributed to TiO_{2-x} after addition of MgO to TiO_2 [33]. For the core-shell sample, the deconvolution of Ti 2p core level yields two major characteristic doublets for $Ti2p_{3/2}$ and $2p_{1/2}$, encompassing a set of two $2p_{3/2}$ peaks at 458.281 eV and 459.267 eV. The 458.281 eV peak is attributed to 3+ state while the 459.267 eV peak is assigned to 4+ valence states of Ti, respectively [54].Similarly the $2p_{1/2}$ peak is also deconvoluted to two peaks at 463.815 eV (3+ state) as well as 465.42 eV (4+state). The occurrence of Ti^{3+} state in the core-shell structure confirms the presence of oxygen vacancy which can be explained as follows. The Ti^{4+} ion near oxygen vacancy accepts an electron from cavity V_0 and yields an F+ center and converts to Ti^{3+} ion.

$$V_o + 2e^- = F$$

$$F + Ti^{4+} = F^+ + Ti^{3+}$$

V_o cavity contains a pair of electrons one of which is occupied by the neighbouring Ti^{4+} ion thus forming an F^+ center. The Mg 2p peak which should be 51.5 eV is shifted to 49 eV. The shifting to lower binding may be due to presence of Mg^{2+} vacancies in the coating MgO layer.

3.7 Optical property analysis

3.7.1 UV-vis absorbtion spectra

Fig. 3.20 shows the UV-Vis absorbance spectra of core TiO_2 annealed at 450^{o}C, 650^{o}C and 850^{o}C along with the corresponding core-shell samples. The maximum absorption peak of TiO_2 appears at 330 nm followed by a big absorption tail in between 350-800

nm. The UV absorption peak is termed as the band to band absorption peak [55-56]. The absorption in the visible region may be due to the presence of Ti $^{3+}$ or oxygen vacancies. In TiO_2 nanoparticles, Ti $^{4+}$ ion is surrounded by six oxygen ions forming basic TiO_6 octahedra. When the system is ambient in oxygen vacancy, loss of oxygen in the lattice releases free electrons. These free electrons are either captured by Ti $^{4+}$ to form Ti $^{3+}$ on the lattice site, to maintain charge neutrality, or got trapped in the oxygen vacancy centers. The electrons captured by the Ti^{4+}, on either side of oxygen vacancy (V_0), forms Ti^{3+}-V_0-Ti^{3+} defect complex, and the electrons trapped by the oxygen vacancies form color centers (F, F^+or F^{++}) [57-58].

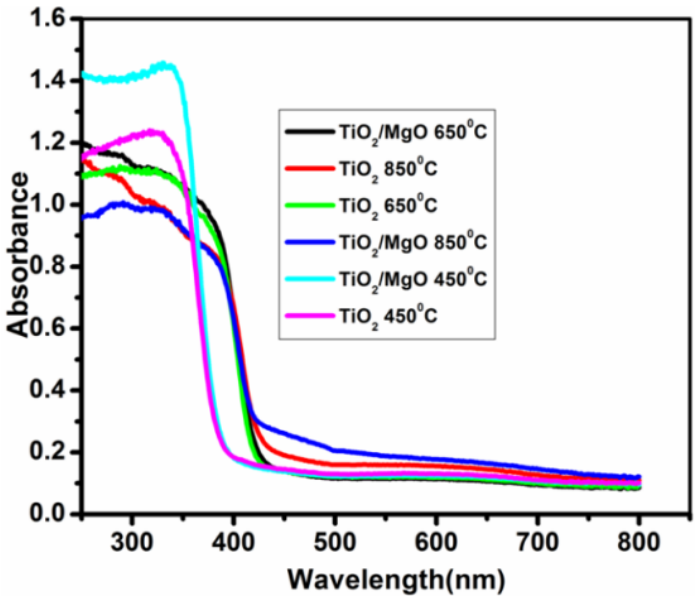

Fig. 3.20 UV-vis absorbance spectra

Oxygen defect related colour centers may show absorption peaks in the range from 2-2.8 eV [57-59]. Apart from colour centers, Ti $^{3+}$ may also show absorptions between 2.2-2.3 eV (539-563 nm) due to 2 T_2 to 2E d-d transition of $d1Ti^{3+}$ [60]. Also the peaks available from 250nm-410 nm (found only in the core-shell structures) may be attributed to addition of MgO as we found in MgO as described in the earlier section, the absorption at 289 nm (4.29 eV) is owing to singlet to singlet $^1A_{1g}$ to ^1E transition of electrons present in the surface F_s center [14]. The other singlet to singlet $^1A_{1g}$ to $^1A_{1g}$ excitation of surface F_s center is observed at 405 nm (3.06 eV).

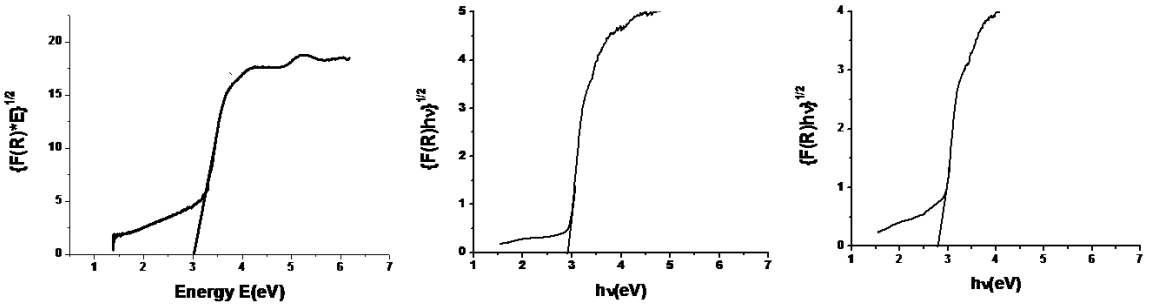

Fig. 3.21 Tauc's Plot for band gap calculation of (left) TM 450, (centre) TM 650 and (right) TM 85

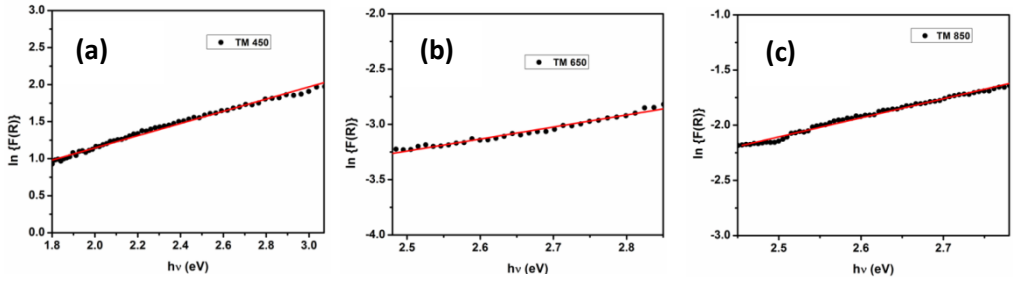

Fig. 3.22 Urbach energy plot (a) TM 450, (b) TM 650 and (c) TM 850

Table 3.3 Calculation of band gap and Urbach energy

Sample name	Urbach energy(eV)	Band gap(eV)
TiO_2 450	0.487	3.25
TM 450	1.213	3.07
TM 650	0.919	2.85
TM 850	0.578	2.75

The band gap calculated from Tauc's plot is presented in table 3.3. Again we know that band gap of MgO is around 7.8 eV. It shows that all core-shell structures are TYPE 2 core-shell structures, which is the most essential criteria for a material to be used in photocatalysis or photovoltaic devices. Also the decrease in band gap suggests that the materials tend to absorb more in the visible region which is another essential

criteria for photoactivity. From the table we can see that there is tremendous increase in Urbach energy when TiO_2 nanoparticles annealed at 450^0C are coated with MgO shell layer. The growth of the shell results in strain and the formation of defect states at the core/shell interface or within the shell [61]. These can act as trap states for photogenerated charge carriers. The excited electrons are captured by the shallow defect bands, preventing their direct transition to the conduction band as a result increasing the Urbach energy to such high extent. In TM 650 where the shell concentration is same as that of TM 450, the Urbach energy decreases as air annealing at a higher temperature fills up the vacant oxygen levels, most of the electrons may undergo excitation to the conduction band instead of getting captured in the defect band. These oxygen defects are mostly accountable for the decrease in the band gap and the magnitude of this gap varies with defect density [62].Same goes for TM 850 as after annealing at such high temperature the amount of oxygen vacancy decreases in the sample subsequently reducing the Urbach energy.

3.7.2 Photoluminescence spectra analysis

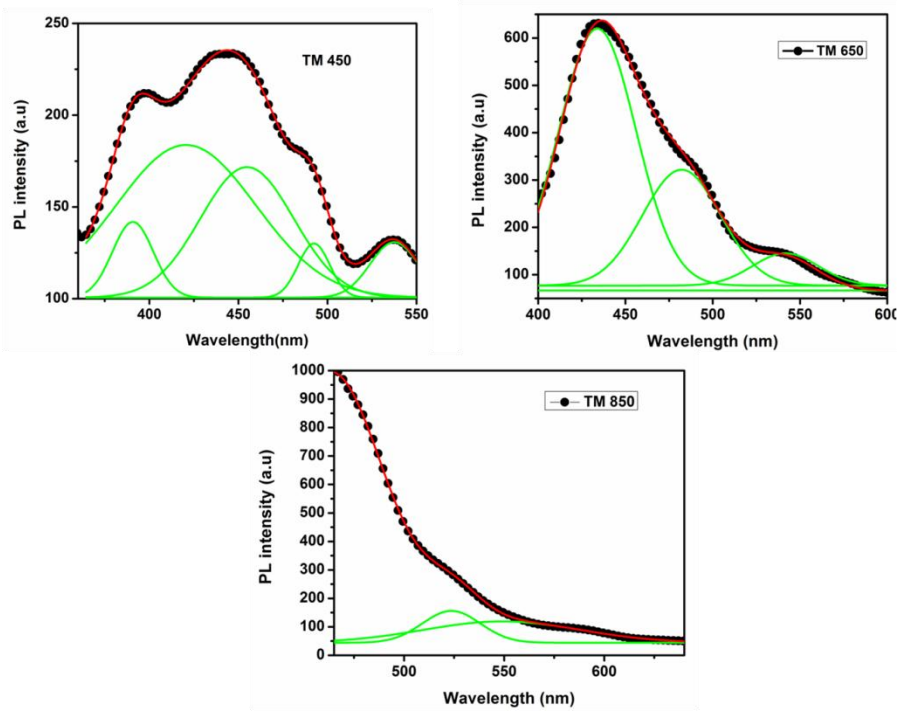

Fig. 3.23 PL spectra of the core-shell nanostructures excited at 350 nm

Fig. 3.23 displays the Gaussian fitted emission spectra of TM 450, TM 650 and TM 850, excited at (350 nm). If we look at the PL spectrum of pure TiO_2 nanoparticle we can see that both core and core-shell TM 450 exhibit an emission peak at 390 nm. This peak corresponds to phonon assisted indirect transition from M→Γ in the Brillouin zone. But it is prominent that the intensity of the peak is suppressed in the core-shell nanostructure. This is due to the outer MgO shell that is covering the core TiO_2 nanoparticles. The lowering of the TiO_2 related UV peak should be due to relatively thick and dense MgO layer, thus the excitation source has low penetration intensity to excite the inner TiO_2 nanoparticles. Again, the photo-generated charge carriers which are emitted from the TiO_2 core are absorbed by the TiO_2 NPs which are formed on the surface of the core.

Although the photo-generated charge carrier emission from the TiO_2 core is very strong, but the TiO_2 NPs which are grown on the surface of TiO_2 core can absorb some of the emission, resulting in the decrease of the UV emission [63].Also from the charge separation diagram we can see that both electron and hole are spatially separated at the interface of the core and shell. This minimizes recombination resulting in decrease of the PL intensity of the peak. All these characteristics lead to TYPE 2 characteristic of the core-shell sample. The visible emission peaks are associated with excitons, oxygen vacancies and different surface defect states [64-66]. Photoluminescence properties of the different crystalline phases depend on their long range crystalline order, as spatial distribution of electron and holes depend on the length of the octahedra chain of the two phases [64-66]. TiO_2 and TM 450 exhibit an intense emission peak around 425 nm which is assigned to self trapped exciton (STE) recombination [68-69] The same peak is shifted to 433 nm in the TM 650 sample. It can be seen that in TM 650 and TM 850, the band edge emission peak is completely diminished. This is mainly due to the decrease in the number of radiative centers, present on the surface or in the bulk phase. Although, oxygen vacancies are found at the interface of the anatase rutile mixed phase TiO_2, those vacancies act as non radiative centers only [73]. Annealing at 950^{o}C removes many of the radiative oxygen vacancy centers, along with non radiative centers thereby completely quenching the

390 nm peak. Oxygen defect related emission peaks occur at 2.67 eV (464 nm) and 2.3 eV (539 nm). These peaks are credited to F or F^{++} and F^{+} centers respectively [67]. The emission peak at 492 nm is due to charge transfer transition from Ti^{3+} to TiO_6^{2} complex, associated with oxygen defects [68-69]

3.7.3 TRPL spectra analysis

Unlike steady state PL, the instrumentation of time resolved PL spectrophotometer uses a pulsed light source for photoexcitation [70]. The time-dependent intensity is measured following the excitation pulse, and decay time is calculated from the slope of a plot of log *I* (*t*) versus *t*, or from the time at which the intensity decreases to 1|*e* of a value at *t* = 0 [71]. Steady state PL analysis of our samples is carried out in Perkin Elmer LS-55 spectrometer with a Xenon light source. The instrument has a scanning range in the visible region spanning from 200-800 nm and the measurement is done at an increment of 0.5 nm. Time resolved photoluminescence (TRPL) spectra are obtained in life spec II spectrofluorssimeter (Edinburgh instrument). The sample was excited by a laser diode of wavelength 342 nm and the decay was measured with a time scale of 2.791736E-11 sec/channel.

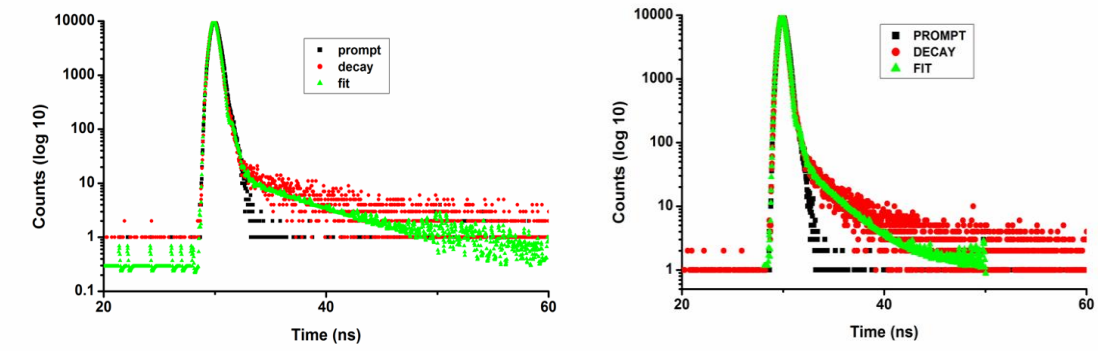

Fig 3.24 TRPL fit of (left) TiO_2 and (right) Core-shell TiO_2-MgO

Fig. 3.24 shows the TRPL spectrum for both core TiO_2 and core-shell TiO_2-MgO nanostructures. A four exponential was fitted to calculate the life time of TiO_2 whilst a five exponential was needed to find out the same for TiO_2-MgO through the following equation

$$y = y_0 + \sum_{i=1}^{n} \alpha_I \exp(-t/\tau_i) \ldots..(\text{for n exponential})$$

From the graph of TiO_2, the values of $\tau_1 = 5.052403E \times 10^{-12}$sec, $\tau_2 = 6.115959 \times 10^{-11}$sec, $\tau_3 = 5.526903 \times 10^{-11}$sec and $\tau_4 = 2.843263 \times 10^{-9}$sec. The values of α_1 = -219.0319, α_2 = -13.22373, α_3= 16.22717and $\alpha_4 = 2.337827 \times 10^{-4}$

The lifetime of core-shell TiO_2-MgO is calculated using the parameters $\tau_1 = 4.953978 \times 10^{-12}$sec, $\tau_2 = 1.405968 \times 10^{-10}$sec, $\tau_3 = 1.276275 \times 10^{-10}$sec, $\tau_4 = 1.28485 \times 10^{-10}$sec, $\tau_5 = 4.901529 \times 10^{-9}$ and α_1 = -156.2194,α_2= 24.9461, α_3 = 447.1461, α_4 = -471.0229, α_5= 1.637182×10^{-4}. The lifetime of electron in the core-shell structure is found to be 0.021 nano sec which is much more higher than that of the core structure that is 0.005 nano sec indicating that there is very less recombination in the sample. This once again stands with the TYPE 2 structure of core-shell TiO_2-MgO. The spatial separation of electron and hole can result in a decrease of the wave function overlap and thus longer lifetime of charge recombination is expected in TYPE 2 like heterostructures. Our observation indicates that the formation of shell leads to an increase in lifetime, which can be concluded as the clear evidence of reduced electron hole wave function overlap in core-shell material. Upon coating the number of oxygen vacancies increases, and therefore large number of carriers are trapped in these defect centers. Therefore, as compared to pure one the electrons in the coated system now transit from one defect to another defect and then to valence band until it find an emission center. The oxygen vacancies, with trapped electrons, act as charged defects. Therefore, these charged oxygen vacancies interact with the mobile electrons and scatter them, thereby decreasing their mobility [72]. Decrease in mobility will separate the electrons-holes for longer time and hence increase the lifetime.

3.8 Photocatalytic Application

Photocatalytic activities of pure TiO_2 nanoparticles and core-shell TiO_2-MgO nanoparticles are examined by observing the degradation of methylene blue (MB) under daylight just as described in chapter 2 (section 2.3.3).

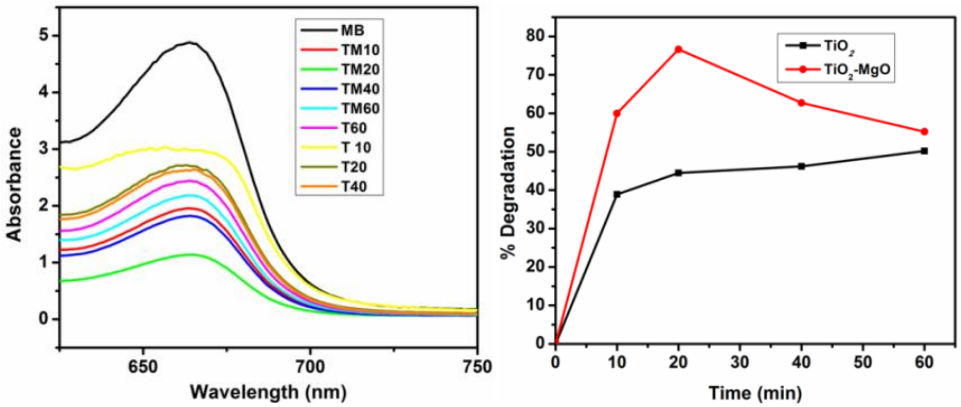

Fig. 3.25 (left) Absorbance of MB in presence of catalyst, (right) %Degradation w.r.t. irradiation time

The degradation efficiency of MB solution is given by$\{ (A_0-A_t)/A_0\}\times100\%$ [2].

Table 3.4: Calculation of %degradation

Sample name	%degradation w.r.t. time			
	10 min	20 min	40 min	60 min
TiO_2	38.9	44.47	46.31	50.2
TiO_2/MgO	59.97	76.64	62.7	55.22

For pristine TiO_2, the maximum degradation efficiency was found as 50.2% while for core-shell TiO_2-MgO nanostructures, the degradations were found to be 76.64% for 20 min irradiation. From this, it is clear that the core-shell nanostructure exhibits much better photocatalytic activity than the core structure. Since the light source has very less energy than to excite TiO_2 (less than 3.2 eV), it requires already created e^--h^+ pair to get them photoexcited. That is why, pure TiO_2 nanoparticles cannot show very good photocatalytic activity. But due to TYPE 2 band allignment, TiO_2-MgO favors charge separation and it can be used as good photocatalytic agent. Also oxygen vacancies act as traps for electron while –OH radicals do the same for holes. From PL, XPS as well as TRPL we have already explained that the number of oxygen vacancy has

significantly increased in the core-shell structure. Again adding MgO coating layer induces more number of hyrdroxyl radicals as we have seen from FTIR. Since the methylene blue solution is prepared in water, upon contact with TiO_2 surface, the H_2O or -OH groups and water dissolved O_2 are adsorbed on different active sites present on the host surface. The electrons trapped in these oxygen vacancies are transferred to the adsorbed oxygen and produce superoxide radicals while the water and hydroxyl ions are converted to its corresponding hydroxyl radical by the photogenerated holes [2-74]. These superoxide and hydroxyl radicals are very strong oxidizing agent and can degrade the dye to its constituent product [75]. Therefore, different possible steps involved in the photodegradation of MB are generation of free electrons and holes, photoexcitation of the dye molecule, trapping of electrons and holes to form superoxide and hydroxyl radicals and finally degradation of the dye. We can see that the degradation is reduced in irradiation time 40 min. This is attributed to lack of charge carriers to degrade the dye although irradiation time is increased; most of the charge carriers generated this way undergo recombination. It is further reduced with increase in irradiation time indicating more charge recombination. The reaction mechanism for TiO_2 to degrade dyes is mentioned below [2].

$$TiO_2 \longrightarrow e^- + h^+$$

$$MB \longrightarrow MB^*$$

$$OH^- + h^+ \longrightarrow OH^\cdot$$

$$O_2 + e^- \longrightarrow O^{2-}$$

3.9 Conclusion

In this chapter, we have discussed about the various spectroscopic and structural characterizations performed on core TiO_2 and core-shell TiO2-MgO nanostructures. It is realized that although TiO_2 nanoparticles have been able to photodegrade the dye Methylene Blue, the efficiency is less than that is exhibited by the core-shell structure. We found that the shell MgO layer highly influences the properties of the core TiO_2, but no distinct evidence of shell characteristics was visible in the optical characterization as we have extensively studied the properties of MgO also to see if

some of them are present in the core-shell structure. This may be due to the fact that MgO has a very high band gap (7.8 eV) which is almost insulating so although it changes the core properties, it fails to leave any sign of itself in the core-shell structure. By comparing the core-shell with its core counterpart, we have seen that the former is ambient in oxygen vacancies which makes it more suitable for the application purpose as we have shown in photocatalysis than the later one.

References

[1] Mahshid, S., et al. Synthesis of TiO_2 nanoparticles by hydrolysis and peptization of titanium isopropoxide solution, *Semicond. Phys. Quantum Electron. Optoelectron.* **9**, 65--68, 2006.

[2] Choudhury, B., et al. Extending photocatalytic activity of TiO_2 nanoparticles to visible region of illumination by doping of cerium, *Photochem. Photobiol.* **88** (2), 257--264, 2012.

[3] Chiodo, L., et al. Self-energy and excitonic effects in the electronic and optical properties of TiO_2 crystalline phases, *Phys. Rev. B: Condens. Matter* **82** (4), 045207-1--045207-12, 2010.

[4] Boubaker, K., et al. A physical explanation to the controversial Urbach tailing universality, *Eur. Phys. J. Plus* **126**, 10, 2011.

[5] Tang, H., et al. Photoluminescence in TiO_2 anatase single crystals, *Solid State commun.* **87** (9), 847--850, 1993.

[6] Yamada, Y., & Kanemitsu, Y. Blue photoluminescence of highly photoexcited rutile TiO2: Nearly degenerate conduction-band effects, *Phys. Rev. B* **82** (11), 113103, 2010.

[7] Wahab, R., et al. Synthesis of Magnesium Oxide Nanoparticles by Sol-Gel Process, *Materials Science Forum* (**558 - 559**), 983--986, 2007.

[8] Feldbach, E., et al. Luminescence spectroscopy of nanocrystalline MgO, *Phys. Status Solidi C***8** (9), 2669--2672, 2011.

[9] Sternig, A., et al. BaO Clusters on MgONanocubes: A Quantitative Analysis of Optical-Powder Properties, *Small* **6** (4), 582--588, 2010.

[10] Shluger, A.L., et al. Spectroscopy of low-coordinated surface sites: Theoretical study of MgO, *Phys. Rev. B: Condens. Matter* **59** (3), 2417--2430, 1999.

[11] Illas, F., & Pacchioni, G. Optical properties of surface and bulk F centers in MgO from ab initio cluster model calculations, *J. Chem. Phys.* **108**, 7835--7841, 1988.

[12] Kumar, A., & Kumar, J. On the synthesis and optical absorption studies of nano-size magnesium oxide powder, *J. Phys. Chem. Solids* **69**(11), 2764--2772, 2008.

[13] Kumar, A., et al. Sol–gel synthesis of highly luminescent magnesium oxide nanocrystallites, *J. Lumin.* **131** (4), 640--648, 2011.

[14] Popov, A.I., et al. Dynamics of F-center annihilation in thermochemically reduced MgO single crystals, *Solid State Commun.* **118** (3), 163--167, 2001.

[15] Boubeta, C.M., et al. Blue luminescence at room temperature in defective MgO films, *Solid State Commun.* **151** (10), 751--753, 2011.

[16] Duley, W.W., &Rosatzin, M. The orange luminescence band in MgO crystals, *J. Phys. Chem. Solids* **46** (2), 165--170, 1985.

[17] Chen, Y., & Abraham, M.M. Trapped-hole centers in alkaline-earth oxides, *J. Phys. Chem. Solids* **51** (7), 747--764, 1990.

[18] Kappers, L.A., et al. F^+ and F' Centers in Magnesium Oxide*, *Phys Rev B: Condens. Matter* **1** (10), 4151--4157, 1970.

[19] Gibson, A., et al. Stability of vacancy defects in MgO: The role of charge neutrality, *Phys. Rev. B: Condens. Matter* **50** (4), 2582--2592, 1994.

[20]Ricci, D., et al. Electron trapping at neutral divacancy sites on the MgO surface, *J. Chem. Phys* **117** (6), 2844--2851, 2002.

[21] Berger, T., et al.The Color of the MgO Surface-A UV/Vis Diffuse Reflectance Investigation of Electron Traps, *J. Phys. Chem. B* **108** (22), 7280--7285, 2004.

[22] Bolton, J.D., et al. Photoluminescence of $F^{2+}{}_2$centres in additively coloured magnesium oxide, *Solid State Commun.* **38** (4), 287--290, 1981.

[23] Zhang, J., & Zhang, L. Intensive green light emission from MgO nanobelts, *Chem. Phys. Lett.* **363**, 293--297, 2002.

[24] Stankic, S., et al. Size-Dependent Optical Properties of MgONanocubes, *Angew. Chem. Int. Ed.* **44** (31), 4917–4920, 2005.

[25] Kawaguchi, Y. Luminescence spectra at bending fracture of single crystal MgO, *Solid State Commun.* **117** (1), 17--20, 2000.

[26] Edel, P., et al. Photoluminescence properties of additively colouredMgO. I. Effects of uniaxial stress and ODMR, *J. Phys. C: Solid State Phys.* **12** (23), 5245--5253, 1979.

[27] Jeffries, B.T., et al. Luminescence in thermochemically reduced MgO: The role of hydrogen, *Phys. Rev. B: Condens. Matter* **25** (3), 2077--2080, 1982.

[28] Uneka, Y., & Uchino, T. Photoexcitation, trapping, and recombination processes of the F-type centers in lasing MgO microcrystals, *Phys. Rev. B: Condens. Matter* **83**, 195108-1--195108-15, 2011.

[29] Gonzalez, R., et al. Photoconversion of F-type centers in thermochemically reduced MgO single crystals, *Phys. Rev. B: Condens. Matter* **59** (7), 4786--4790, 1999.

[30] R. Gonzalez, M.A. Monge, J.E.M. Santiuste, R. Pareja, Y. Chen, E. Kotomin, M.M. Kukla, A.I. Popov, Phys. Rev. B: Condens. Matter **59**, 4786, 1999.

[31] Avellaneda. C. O., et al. Preparation and characterization of core-shell electrodes for application in gel electrolyte-based dye-sensitized solar cells, *Electrochimica Acta* **55**, 1468--1474, 2010

[32] Choudhury, B., et al. Defect generation, d-d transition, and band gap reduction in Cu-doped TiO_2 nanoparticles, *Int. NanoLett.* **3** (25), 1--8, 2013.

[33] Chetri, P., et al. Exploring the structural and magnetic properties of TiO_2/SnO_2 core/shell nanocomposite: An experimental and density functional study, *J. Solid State Chem.* **220**, 124--131, 2014.

[34]Jung, H.S., et al. Enhancing photocatalytic activity by using TiO_2–MgO core-shell-structured nanoparticles, *Appl. Phys. Lett.* **88** (1), 013107-1--013107-3, 2006.

[35] Kaufmann, E.N. (ed.). *Characterization of Materials*, John Willey & Sons, New Jersey, 2003.

[36] Banwell, C. & McCash, E.M. *Fundamentals of molecular spectroscopy*, 4th ed., Tata McGraw-Hill education, New Delhi, 2012.

[37] Hosokawa, M., Nogi, K., Naito, M., & Ykoyama, T. *Nanoparticle Technology Handbook*, Elsevier, Oxford, 2007.

[38] Willard, H.H., Meritt, L.L., Dean, J.A., & Settle, F.A. *Instrumental methods of analysis*, 7th ed., CBS publishers, New Delhi, 2009.

[39] Choudhury, B., & Choudhury, A. Dopant induced changes in structural and optical properties of Cr doped TiO_2 nanoparticles, *Mater. Chem. Phys.***132** (2-3), 1112--1118, 2012.

[40] Brojcin, M.G., et al. Infrared study of laser synthesized anatase TiO_2nanopowders, *J. Phys. D: Appl. Phys.* **38** (9), 1415--1420, 2005.

[41] Zhang, W.F., et al. Raman scattering study of anatase TiO_2nanocrystals, *J. Phys. D: Appl. Phys.***33** (8), 912-916, 2000.

[42] Zhang, J., et al. UV Raman spectroscopic study on TiO_2: I: Phase transformation at the surface and in the bulk, *J. Phys. Chem. B* **110** (2), 927--935, 2006.

[43] Georgescu, D., et al. Experimental assessment of the phonon confinement in TiO_2anatasenanocrystallites by Raman spectroscopy, *J. Raman Spect.* **43** (7), 876--883, 2012.

[44] Sahoo, S., et al. Raman line shapes of optical phonons of different symmetries in anatase TiO_2nanocrystal, *J. Phys. Chem. C* **113** (39), 16927--16933, 2009.

[45] Mali, S.M., et al. Hydrothermal synthesis of rutile TiO_2 with hierarchical microspheres and their characterization, *Cryst. Engg. Comm.* **13**, 6349--6351, 2011.

[46] Skryshevskyy, V.A., et al. Infrared-active defects in a TiO_2 mixture of coexisting anatase and rutile phases, *Phys. Stat. Sol. A* **201** (1), 157--161, 2004.

[47] Zhu, K.R., et al. Size and phonon-confinement effects on low-frequency Raman mode ofanatase TiO_2nonocrystal, *Phys. Lett. A* **340** (1-4), 220--227, 2005.

[48] Xu, C.Y., et al. Blue shift of Raman peak from coated TiO_2 nanoparticles, *J. Raman Spectrosc.* **32** (10), 862--65, 2001.

[49]Nie, A., et al. Epitaxial TiO_2/SnO_2 core–shell heterostructure by atomic layer deposition, *J. Mater. Chem.* **22**, 10665--10671, 2012.

[50] Das, K., et al. Morphology Dependent Luminescence Properties of Co Doped TiO_2 Nanostructures, *J. Phys. Chem C* **113** (33), 14783--14792, 2009.

[51] Wang, D., et al. Lattice vibration fundamentals in nanocrystallineanatase investigated with Raman scattering, *J. Phys.: Condens. Matter* **20** (8), 085212, 2008.

[52] Zhang, H., & Banfield, J.F. Phase transformation of nanocrystalline anatase-torutile via combined interface and surface nucleation, *J. Mater. Res.* **15** (2), 437--448, 2000.

[53] Muilenberg, G.E., Riggs, W.H., Davis, L.E., Moulder, J.F., &Muilenberg, G.E. (ed.). *Handbook of X-ray Photoelectron Spectroscopy*, Perkin Elmer Cooperation, Eden Prairie, MN, 1979.

[54] Santara, B., et al. Evidence of oxygen vacancy induced room temperature ferromagnetism in solvothermally synthesized undoped TiO_2 nanoribbons, *Nanoscale* **5**, 5476--5488, 2013.

[55] Choudhury, B., et al. Ce-Ndcodoping effect on the structural and optical properties of TiO_2 nanoparticles, *Mater. Sci. Eng. B* **178** (4), 239--247, 2013.

[56] Mo, S.D., & Ching, W.Y. Electronic and optical properties of three phases of titanium dioxide: Rutile, anatase, and brookite, *Phys Rev. B: Condens. Matter* **51** (19), 13023--13032, 1995.

[57] Komaguchi, K., et al. Electron transfer reaction of oxygen species on TiO_2 nanoparticles induced by sub-band-gap illumination, *J. Phys. Chem. C* **114** (2), 1240--1245, 2010.

[58] Kuznetsov, V.N., &Serpone, N. On the origin of spectral bands in the visible absorption spectra of visible-light-active TiO_2 specimens analysis and assignments, *J. Phys. Chem. C* **113** (34), 15110--15123, 2009.

[59] Kuznetsov, V.N., &Krutitskaya, T.K. Nature of color centers in reduced titanium dioxide, Kinet. Catal. 37 (3), 446--449, 1996.

[60] Sekiya, T., et al. Absorption spectra of anatase TiO_2 single crystals heat-treated under oxygen atmosphere, *J. Phys. Chem. Solid.* **61** (8), 1237--1242, 2000.

[61] Reiss, P., et al. Core/Shell Semiconductor Nanocrystals, *Small* **5** (2), 154--168, 2009.

[62] Q. Zhong, J. M. Vohs, D. A. Bonnel, Effect of reduction on the topographic and electronic structure of TiO2 (110) surfaces, *Surf. Sci.* **274** (1) 35--43, 1992.

[63] Sookhakianan , M., et al. Synthesis, structural, and optical properties of type-II ZnO–ZnS core–shell nanostructure , *J. Lumin.* **145**, 244--252, 2014

[64] Tang, H., et al. Photoluminescence in TiO_2 anatase single crystals, *Solid State commun.* **87** (9), 847-850, 1993.

[65] Yamada, Y., & Kanemitsu, Y. Blue photoluminescence of highly photoexcitedrutile TiO_2: nearly degenerate conduction-band effects, *Phys. Rev. B: Condens. Matter* **82** (11), 113103-1--113103-4, 2010.

[66] Preclikova, J., et al. Nanocrystalline titanium dioxide films: Influence of ambientconditions on surface- and volume-related photoluminescence, *J. Appl. Phys.* **108** (11), 113502-1--113502-7, 2010.

[67] Lei, Y., et al. Preparation and photoluminescence of highly ordered TiO_2 nanowire arrays, *Appl. Phys. Lett.* **78** (8), 1125--1127, 2001.

[68] Liu, J., et al. Structure and photoluminescence study of TiO_2nanoneedle texture along vertically aligned carbon nanofiber arrays, *J. Phys. Chem. C* **112** (44), 17127--17132, 2008.

[69] Yu, J.C., et al. Effects of F- doping on the photocatalyticactivity and microstructures of nanocrystalline TiO_2 powders, *Chem. Mater.* **14** (9), 3808--3816, 2002.

[70] Kaufmann, E.N. (ed.). Characterization of Materials, John Willey & Sons, New Jersey, 2003.

[71] Gaft, M., & Reisfeld, R. Modern luminescence spectroscopy of minerals and materials, Springer, New York, 2005.

[72] Wang, X., et al. Trap states and carrier dynamics of TiO2 studied by photoluniscence spectroscopy under weak excitation condition, *Phys. Chem. Chem. Phys.* **12** (26), 7083--7090, 2010.

[73]Choudhury, B., and Choudhury,A., Local structure modification and phase transformation of TiO_2 nanoparticles initiated by oxygen defects, grain size, and annealing temperature, *International Nano Letters* **3**, 55(1--9), 2013.

[74] Bingham, S., &Daoud, W.A. Recent advances in making nano-sized TiO_2 visible-light active through rare earth metal doping, *J. Mater. Chem.* **21** (7), 2041--2050, 2011.

[75] Parida, K.M., &Sahu, N. Visible light induced photocatalytic activity of rare earth titaniananocomposites, *J. Mol. Catal. A: Chem.* **287** (1-2), 151--158, 2008.